High-order harmonic generation in orthogonal IR and XUV pulses: XUV-initiated channel separation and polarization control

T. S. Sarantseva [1,2] A. A. Romanov [1] A. A. Silaev [1] N. V. Vvedenskii [1] and M. V. Frolov [1,2]
[1]*Department of Radiophysics, University of Nizhny Novgorod, Nizhny Novgorod 603950, Russia*
[2]*Department of Physics, Voronezh State University, Voronezh 394018, Russia*

(Received 20 September 2022; revised 25 January 2023; accepted 7 February 2023; published 22 February 2023)

Single-atom high-order harmonic generation (HHG) induced by an intense linearly polarized infrared (IR) field and assisted by a perturbative extreme ultraviolet (XUV) short pulse with linear polarization is analyzed in perpendicular geometry. It is shown that for the case of the initial p state, the two independent projections of the laser-induced dipole are formed by two independent physical channels, which are responsible for IR-induced HHG and XUV-initiated HHG. This property of the laser-induced dipole is utilized for polarization control of the generated radiation. An alternative scheme for studying XUV-initiated HHG is proposed.

DOI: 10.1103/PhysRevA.107.023113

I. INTRODUCTION

High-order harmonic generation (HHG) in atomic and molecular medium attracts enduring attention due to a wide range of practical applications: Generation of coherent light in the extreme ultraviolet (XUV) region [1–3], attosecond pulse generation [4–6], HHG-based spectroscopy [7–9], etc. Most of these applications are based on the plateau effect in the HHG spectrum, which can be interpreted within the well-known three-step scenario [10], which splits HHG into three steps: (i) laser-field-induced tunneling of an atomic electron, (ii) propagation of the liberated electron in the laser-dressed continuum along a closed classical trajectory, and (iii) electron recombination to the initial state with the emission of a high-energy photon (harmonic). The validity of the three-step scenario is limited by an intense low-frequency field, which ensures the applicability of semiclassical approximation for HHG description [11–14]. Different configurations of the low-frequency field are used in HHG experiments aiming to extend the high-energy plateau [1–3], increase the HHG conversation efficiency [15], and control the polarization properties of emitted harmonics [16–18].

In the past decade, the theoretical and experimental interests in the HHG process were extended to the study of so-called XUV-induced HHG, for which IR-induced HHG is affected by high-frequency pulse or pulse trains with the carrier frequency in the XUV range. The additional perturbative XUV field induces new HHG channels led by modification of recombination and ionization steps of HHG. One of these channels originates from the absorption of XUV photons at the moment of recombination, resulting in the formation of a second XUV-induced plateau with an extended cutoff [19,20]. Harmonics on the additional plateau can be utilized for several practical applications such as HHG-based spectroscopy [20], attosecond pulse metrology [21,22], and visualization of contributing closed classical trajectories in the IR field [23]. Although the XUV-assisted HHG channel shows a wide range of practical applications, its utilization is limited by the small magnitude of the corresponding HHG amplitude. The other, more intense channel is led by single XUV photon ionization, thereby initiating the HHG process by placing the atomic electron in the IR-dressed continuum [24–28]. The XUV-initiated ionization step leads to the formation of a new set of closed electron trajectories which bring the electron back to the atomic residue with slightly smaller energy than the electron can gain in an intense IR field starting with zero initial velocity. In order to separate the XUV-initiated HHG channel from other channels, comparatively low intensity of the IR field is used in actual experiments [26–28]. Lowering the intensity of the IR field drastically decreases the tunneling probability, thereby ensuring the dominant contribution of the XUV-initiating channel. We note that the XUV-induced HHG experiment is performed by utilizing harmonics generated by an intense IR field [25,27–29]. However, the recent progress in the shaping and pulse-to-pulse stabilization of subfemtosecond and attosecond XUV pulses from free electron laser (FEL) sources [30] opens a new avenue for using FEL-based attosecond pulse sources in HHG experiments [31].

In this work, we consider single-atom XUV-induced HHG with an intense IR field and perturbative attosecond XUV pulse. Two pulses are linearly polarized in two mutually perpendicular directions. Within this geometry of the XUV-induced HHG, we suggest an alternative way to separate the XUV-initiated HHG channel from other channels based on the features, which are initiated by the interaction of a two-component field with an atomic electron having nonzero angular momentum in an initial state. We also discuss the polarization control of the generated harmonics through the variation of time delay between IR and attosecond pulses.

This paper is organized as follows. In Sec. II we discuss the theoretical background for XUV-initiated HHG: In Sec. II B XUV-initiated HHG amplitude is considered in the adiabatic approximation, and Sec. II C considers initial state symmetry effects for XUV-initiated ionization and recombination.

Numerical results and their discussions are presented in Sec. III. Our work is summarized in Sec. IV. Atomic units are used throughout this article if not specified otherwise.

II. THEORETICAL BACKGROUND

A. Laser field and initial state

We consider an atomic system in a two-component field consisting of an intense low-frequency field and a time-delayed high-frequency pulse. Both components are linearly polarized in orthogonal directions:

$$\boldsymbol{F}(t) = \hat{\boldsymbol{x}} F_{\mathrm{IR}}(t) + \hat{\boldsymbol{y}} F_{\mathrm{XUV}}(t-\tau), \tag{1}$$

where τ is the time delay between the two pulses. The electric field for both pulses can be parametrized in terms of the envelope $[f_\alpha(t)]$, peak strength (F_α), carrier frequency (ω_α), and carrier-envelope phase (CEP) (ϕ_α):

$$F_\alpha(t) = F_\alpha f_\alpha(t)\cos(\omega_\alpha t + \phi_\alpha), \tag{2}$$

where $\alpha = \mathrm{IR}$ or XUV for IR or XUV pulse, respectively. We assume that the carrier frequency of the low-frequency component belongs to the IR spectral region, and the Keldysh parameter corresponding to the IR component is small, $\gamma_{\mathrm{IR}} = \omega_{\mathrm{IR}}\kappa/F_{\mathrm{IR}} \ll 1$ ($\kappa = \sqrt{2I_p}$, where I_p is the ionization potential). The smallness of γ_{IR} allows one to treat the interaction of the IR field with the atomic target semiclassically. We also assume that the high-frequency component belongs to the XUV region so that its carrier frequency exceeds the ionization potential of the atomic system, $\omega_{\mathrm{XUV}} > I_p$. The application of the perturbation theory in the XUV field is managed by the smallness of parameter $\beta_{\mathrm{XUV}} = F_{\mathrm{XUV}}/(\omega_{\mathrm{XUV}}^2 a) \ll 1$, where a is the spatial scale of the atomic system [32–34]. It should be noted that the perturbation theory regime is realized up to comparatively high intensity ($\sim 10^{15}\,\mathrm{W/cm^2}$ for noble gas atoms). Finally, intensities and carrier frequencies of the considered IR and XUV fields ensure the validity of the dipole approximation, i.e., (i) the laser-induced electron velocity, which characterizes the energetics of a nonlinear process in a strong laser field, is much less than the speed of light, so that the effects induced by the magnetic component of the laser field are negligible; and (ii) the wavelength of the XUV pulse is considerably larger than the atomic scale a, so that spatial nonhomogeneity of the XUV field is not important.

In this work, we assume that the active electron is initially bound in the p state, which is triple degenerate in angular momentum projection m. For a free atom, the atomic state is characterized by the binding energy ($E_0 = -I_p$), angular momentum ($l = 1$), and its projection (m), while the laser field having two spatial projections can couple different magnetic sublevels and classification of an initial state in terms of single magnetic projection may not be appropriate (see discussion for the elliptically polarized field in Refs. [35,36] and for the two-color field in Ref. [37]). For the laser field having two independent spatial projections [see, e.g., Eq. (1)], the more appropriate basis for angular dependence of an initial state is the set of real tesseral spherical harmonics, which are presented by a linear combination of spherical functions [38]. For $l = 1$, these functions are

$$f_0(\hat{\boldsymbol{r}}) = Y_{10}(\hat{\boldsymbol{r}}), \tag{3a}$$

$$f_q(\hat{\boldsymbol{r}}) = i^{\frac{3-q}{2}} \frac{Y_{1,1}(\hat{\boldsymbol{r}}) + qY_{1,-1}(\hat{\boldsymbol{r}})}{\sqrt{2}},\ q = \pm 1, \tag{3b}$$

where $q = 0, \pm 1$ is the polarization index.[1] The functions (3) are unity normalized and orthogonal to each other and can be used as a counterpart of spherical functions for the case of the absence of the cylindrical symmetry, i.e., in the case of not conserved m.

We present the wave function of an optical electron in the absence of the laser field as a product of the radial part and angular one determined by Eq. (3):

$$\psi_q(\boldsymbol{r}, t) = \varphi_q(\boldsymbol{r}) e^{iI_p t},\ \varphi_q(\boldsymbol{r}) = \phi_0(r) f_q(\hat{\boldsymbol{r}}). \tag{4}$$

For large distances ($\kappa r \gg 1$), the function $\phi_0(r)$ decreases exponentially,

$$\phi_0(r) \approx C_\kappa r^{Z/\kappa - 1} e^{-\kappa r}, \tag{5}$$

where C_κ is the asymptotic coefficient and Z is the charge of an atomic residue. It is worth noting that the state with fixed polarization index q is aligned in space along a corresponding Cartesian axis.

B. HHG amplitude within adiabatic approximation

Amplitude for generated harmonic of frequency Ω and polarization vector $\boldsymbol{e}_h$ is determined by the expression

$$\mathcal{A}(\Omega; \boldsymbol{e}_h) = (\boldsymbol{e}_h^* \cdot \boldsymbol{\mathcal{D}}(\Omega)), \tag{6}$$

where $\boldsymbol{\mathcal{D}}(\Omega)$ is the laser-induced dipole moment at the frequency Ω. For the initially unpolarized atom, all aforementioned states may be equally populated, so that the laser-induced dipole moment $\boldsymbol{\mathcal{D}}(\Omega)$ should be averaged in polarization states,

$$\boldsymbol{\mathcal{D}}(\Omega) = \frac{1}{3} \sum_{q=0,\pm 1} \boldsymbol{\mathcal{D}}_q(\Omega), \tag{7}$$

where $\boldsymbol{\mathcal{D}}_q(\Omega)$ is the laser-induced dipole for a given polarization state q. Our theoretical analysis is limited by the first order of the perturbation theory in the XUV field. Moreover, from all channels induced by XUV pulse in the first order, we consider only one associated with XUV-initiated HHG [25,27–29]. Within these approximations, the dipole $\boldsymbol{\mathcal{D}}_q(\Omega)$ can be further expanded in series over F_{XUV},

$$\boldsymbol{\mathcal{D}}_q(\Omega) = \boldsymbol{\mathcal{D}}_{0,q}(\Omega) + \boldsymbol{\mathcal{D}}_{1,q}(\Omega), \tag{8}$$

where $\boldsymbol{\mathcal{D}}_{n,q} \propto F_{\mathrm{XUV}}^n$ for $n = 0,\ 1$. The explicit form of the dipole matrix element $\boldsymbol{\mathcal{D}}_{n,q}$ for $n = 0$ was discussed in

[1] The quantize axis is the z axis.

Ref. [13] and for $n = 1$ in Ref. [14]:

$$\mathcal{D}_{0,q}(\Omega) = \sum_j a_q^{(\mathrm{tun})}(\tilde{t}_j, \tilde{t}'_j) g^{(\mathrm{pr})}(\tilde{t}_j, \tilde{t}'_j) \boldsymbol{d}_q^{(\mathrm{rec})}(\tilde{\boldsymbol{K}}_j), \quad (9)$$

$$\mathcal{D}_{1,q}(\Omega) = F_{\mathrm{XUV}} e^{i(\omega_{\mathrm{XUV}}\tau - \phi_{\mathrm{XUV}})} \times \sum_j f_{\mathrm{XUV}}(t'_j - \tau) a_q^{(\mathrm{ion})}(t_j, t'_j) g^{(\mathrm{pr})}(t_j, t'_j) \times \boldsymbol{d}_q^{(\mathrm{rec})}(\boldsymbol{K}_j), \quad (10)$$

where $\tilde{t}'_j$ and $\tilde{t}_j$ (t'_j and t_j) are ionization and recombination times for IR-induced (XUV-initiated) HHG, and the vectors $\tilde{\boldsymbol{K}}_j \equiv \boldsymbol{K}(\tilde{t}_j; \tilde{t}_j, \tilde{t}'_j)$ and $\boldsymbol{K}_j \equiv \boldsymbol{K}(t_j; t_j, t'_j)$ are expressed in terms of auxiliary vector $\boldsymbol{K}(\tau'; t, t')$:

$$\boldsymbol{K}(\tau'; t, t') = \hat{\boldsymbol{x}} K(\tau'; t, t'), \quad (11a)$$

$$K(\tau'; t, t') = A_{\mathrm{IR}}(\tau') - \frac{1}{t - t'} \int_{t'}^{t} A_{\mathrm{IR}}(\tau'') d\tau'', \quad (11b)$$

$$A_{\mathrm{IR}}(t) = -\int^{t} F_{\mathrm{IR}}(\tau') d\tau'. \quad (11c)$$

The factors $a_q^{(\mathrm{tun})}$ and $a_q^{(\mathrm{ion})}$, $g^{(\mathrm{pr})}$ and $\boldsymbol{d}_q^{(\mathrm{rec})}(\boldsymbol{K}_j)$ describe ionization, propagation, and recombination steps in the three-step scenario [10]. We note that since the interaction of an atomic system with the XUV field is considered as a perturbation, the laser-induced dynamics in the IR-dressed continuum is steered only by the IR field, thereby ensuring the identical structure of propagation factors for $\mathcal{D}_{0,q}$ and $\mathcal{D}_{1,q}$.

The factor $a_q^{(\mathrm{tun})}$ is given by the tunneling exponential factor

$$a_q^{(\mathrm{tun})}(\tilde{t}_j, \tilde{t}'_j) = C_\kappa Q_j \frac{e^{-\kappa^3/(3\tilde{F}_j)}}{\sqrt{\kappa \tilde{F}_j}} f_q(\boldsymbol{e}_j), \quad (12)$$

where C_κ is the asymptotic coefficient (5), $\tilde{F}_j$ is the magnitude of the IR field strength at the moment of ionization, $\tilde{F}_j = |\boldsymbol{F}_{\mathrm{IR}}(\tilde{t}'_j)|$, $\boldsymbol{e}_j$ is the complex vector

$$\boldsymbol{e}_j = i \frac{\dot{\tilde{\boldsymbol{K}}}'_j}{\tilde{F}_j}, \quad \dot{\tilde{\boldsymbol{K}}}'_j = \frac{\partial \tilde{\boldsymbol{K}}'_j}{\partial \tilde{t}'_j}, \quad (13)$$

where $\tilde{\boldsymbol{K}}'_j \equiv \boldsymbol{K}(\tilde{t}'_j; \tilde{t}_j, \tilde{t}'_j)$ is electron momentum at the moment of ionization, and Q_j is the Coulomb factor [39].

The ionization factor $a_q^{(\mathrm{ion})}(t_j, t'_j)$ is given by the dipole transition matrix element describing the transition from the bound state $\psi_q(\mathbf{r}, t)$ to the continuum state $\psi_{\boldsymbol{K}'_j}^{(+)}(\boldsymbol{r})$ through the absorption of the XUV photon:

$$a_q^{(\mathrm{ion})}(t_j, t'_j) = -\frac{(\boldsymbol{d}_q(\boldsymbol{K}'_j) \cdot \boldsymbol{e}_{\mathrm{XUV}}) e^{-i\omega_{\mathrm{XUV}} t'_j}}{2\pi \sqrt{\boldsymbol{K}'_j \cdot [\boldsymbol{F}_j + \boldsymbol{K}'_j/(t_j - t'_j)]}}, \quad (14)$$

$$\boldsymbol{d}_q(\boldsymbol{k}) = \langle \psi_{\boldsymbol{k}}^{(+)}(\boldsymbol{r}) | \boldsymbol{r} | \varphi_q(\boldsymbol{r}) \rangle, \quad (15)$$

where $\boldsymbol{K}'_j = \boldsymbol{K}(t'_j; t_j, t'_j)$, and $\boldsymbol{F}_j = \boldsymbol{F}_{\mathrm{IR}}(t'_j)$. We note that, since we assume that $\boldsymbol{e}_{\mathrm{XUV}} = \hat{\boldsymbol{y}}$, the ionization factor $a_q^{(\mathrm{ion})}(t_j, t'_j)$ is determined by the y component of the transition dipole (15).

The propagation factor $g^{(\mathrm{pr})}(t, t')$ is determined by the classical action $S(t, t')$ of the electron gained in an intense IR field between the two time instants t' and t:

$$g^{(\mathrm{pr})}(t, t') = \frac{e^{-iS(t,t') + i\Omega t}}{(t - t')^{3/2}}, \quad (16)$$

$$S(t, t') = \frac{1}{2} \int_{t'}^{t} \boldsymbol{K}^2(\tau'; t, t') d\tau' + I_p(t - t'). \quad (17)$$

The recombination matrix element $\boldsymbol{d}_q^{(\mathrm{rec})}(\boldsymbol{k})$ is given by

$$\boldsymbol{d}_q^{(\mathrm{rec})}(\boldsymbol{k}) = \boldsymbol{d}_q^*(\boldsymbol{k}) = \langle \varphi_q(\boldsymbol{r}) | \boldsymbol{r} | \psi_{\boldsymbol{k}}^{(+)}(\boldsymbol{r}) \rangle, \quad (18)$$

where $\boldsymbol{k} = \tilde{\boldsymbol{K}}_j$ for the IR-induced channel and $\boldsymbol{k} = \boldsymbol{K}_j$ for the XUV-initiated HHG channel.

The real ionization and recombination times in the absence of the XUV pulse ($\tilde{t}'_j$ and $\tilde{t}_j$) are found from the system of nonlinear equations [13],

$$K(\tilde{t}'_j; \tilde{t}_j, \tilde{t}'_j) = 0, \quad (19a)$$

$$\boldsymbol{K}^2(\tilde{t}_j; \tilde{t}_j, \tilde{t}'_j) = 2(\Omega - I_p) + \Delta E, \quad (19b)$$

where ΔE is given by

$$\Delta E = \frac{\kappa^2}{\tilde{t}_j - \tilde{t}'_j} \frac{K(\tilde{t}_j; \tilde{t}_j, \tilde{t}'_j)}{F_{\mathrm{IR}}(\tilde{t}'_j)}.$$

This system of equations shows that the electron liberates from an atom with zero momentum at the instant $\tilde{t}'_j$ [see Eq. (19a)] and propagates along closed classical trajectories up to moment $\tilde{t}_j$ with some energy gained from the IR field, which is emitted by the electron as a photon with energy Ω through the recombination [see Eq. (19b)].

The corresponding system of nonlinear equations for pair of times t_j and t'_j is

$$\boldsymbol{K}^2(t'_j; t_j, t'_j) = 2(\omega_{\mathrm{XUV}} - I_p), \quad (20a)$$

$$\boldsymbol{K}^2(t_j t_j, t'_j) = 2(\Omega - I_p). \quad (20b)$$

The system (20) describes the three-step scenario for the XUV-initiated HHG channel: The electron escapes from an atom by a single XUV photon ionization by getting nonzero initial momentum in the continuum [see Eq. (20a)], which allows the electron to propagate along a closed classical trajectory up to moment t_j, with subsequent emission of gained in IR field energy through the recombination photon with energy Ω [see Eq. (20b)]. We note that the maximum gained energy for the XUV-initiated HHG channel is smaller than in the IR-induced one.

It should be mentioned that propagation factor $g^{(\mathrm{pr})}$ originates from the electron motion in an intense IR field and does not depend on the atomic structure, while ionization and recombination factors significantly depend on the atomic structure and spacial symmetry of an initial state, which we discuss in turn.

C. Initial state symmetry effects in ionization and recombination steps

We start our analysis from the ionization step of the HHG process. For the IR-induced HHG (corresponding to the zero order of perturbation theory in the XUV field), the impact of the initial state symmetry is enclosed in the form factor $f_q(\boldsymbol{e}_j)$ [see Eq. (12)]. For the field (1), this form factor differs from

zero only for $q=-1$, since $\tilde{\boldsymbol{K}}'_j=\hat{\boldsymbol{x}}\tilde{K}'_j$ and the vector $\boldsymbol{e}_j$ has only one x component [see Eq. (13)].

In order to obtain the general result for $\boldsymbol{d}_q(\boldsymbol{k})$ in terms of the principal vectors of the problem, we consider the dipole transition matrix element from the state having zero projection of angular momentum on the quantized axis. For $q=0$, the quantized axis coincides with the z axis. The transition dipole amplitude from the initial state with $m=0$ can be presented in terms of the irreducible tensor product [38,40]

$$\boldsymbol{d}_0(\boldsymbol{k})\cdot\boldsymbol{e}=\sum_{l=0,2}A_l\{Y_l(\hat{\boldsymbol{k}})\otimes\boldsymbol{e}\}_{1,0}. \tag{21}$$

Coefficients A_l are proportional to the radial matrix elements

$$A_l=C^{10}_{10,l0}\sqrt{\frac{2l+1}{3}}D_l, \tag{22}$$

$$D_l(k)=\langle R_{k,l}|r|\phi_0(r)\rangle, \tag{23}$$

where $C^{10}_{10,l0}$ is the Clebsch-Gordan coefficient, and $R_{k,l}$ is the radial part of the continuum wave function

$$\psi^{(+)}_{\boldsymbol{k}}(\boldsymbol{r})=\sum_{l,m}R_{k,l}(r)Y^*_{l,m}(\theta_k,\phi_k)Y_{l,m}(\theta,\phi). \tag{24}$$

The tensor products in Eq. (21) can be represented as [38]

$$\{Y_0(\hat{\boldsymbol{k}})\otimes\boldsymbol{e}\}_{1,0}=\sqrt{\frac{1}{4\pi}}(\boldsymbol{e}\cdot\hat{\boldsymbol{z}}),$$

$$\{Y_2(\hat{\boldsymbol{k}})\otimes\boldsymbol{e}\}_{1,0}=\sqrt{\frac{15}{8\pi}}\{\{\hat{\boldsymbol{k}}\otimes\hat{\boldsymbol{k}}\}_2\otimes\boldsymbol{e}\}_{10}$$

$$=\frac{1}{\sqrt{2}}[(\boldsymbol{e}\cdot\hat{\boldsymbol{z}})-3(\hat{\boldsymbol{k}}\cdot\boldsymbol{e})(\hat{\boldsymbol{k}}\cdot\hat{\boldsymbol{z}})].$$

Using definitions (22), one can transform the transition dipole to the form

$$\boldsymbol{d}_0(\boldsymbol{k})=\sqrt{\frac{3}{4\pi}}\left[\frac{D_0(k)-D_2(k)}{3}\hat{\boldsymbol{z}}+D_2(k)\frac{(\boldsymbol{k}\cdot\hat{\boldsymbol{z}})}{k^2}\boldsymbol{k}\right]. \tag{25}$$

The ionization factor in Eq. (14) contains the dipole transition elements $\boldsymbol{d}_q(\boldsymbol{K}')$, which we obtain from Eq. (25) by substituting $\boldsymbol{k}\to\boldsymbol{K}'_j$ and $\hat{\boldsymbol{z}}\to\hat{\boldsymbol{y}}$ for $q=+1$ and $\hat{\boldsymbol{z}}\to\hat{\boldsymbol{x}}$ for $q=-1$,

$$\boldsymbol{d}_{+1}(\boldsymbol{K}'_j)=\sqrt{\frac{3}{4\pi}}\left[\frac{D_0(K'_j)-D_2(K'_j)}{3}\hat{\boldsymbol{y}}+D_2(K'_j)\frac{(\boldsymbol{K}'_j\cdot\hat{\boldsymbol{y}})}{K'^2_j}\boldsymbol{K}'_j\right], \tag{26a}$$

$$\boldsymbol{d}_{-1}(\boldsymbol{K}'_j)=\sqrt{\frac{3}{4\pi}}\left[\frac{D_0(K'_j)-D_2(K'_j)}{3}\hat{\boldsymbol{x}}+D_2(K'_j)\frac{(\boldsymbol{K}'_j\cdot\hat{\boldsymbol{x}})}{K'^2_j}\boldsymbol{K}'_j\right]. \tag{26b}$$

Since $\boldsymbol{K}'$ is directed along the x axis [see Eq. (11a)], $\boldsymbol{K}'=\hat{\boldsymbol{x}}\tilde{K}'$, the transition dipole $\boldsymbol{d}_{-1}(\boldsymbol{K}')$ has only an x component. The ionization factor (14) is determined by the y component of the dipole matrix element, so that it turns to zero for the state with $q=-1$, while for the state with $q=+1$ the transition dipole $\boldsymbol{d}_{+1}(\boldsymbol{K}')$ has the nonzero y component

$$d_{+1,y}=\sqrt{\frac{3}{4\pi}}\frac{D_0(K'_j)-D_2(K'_j)}{3}, \tag{27}$$

determining nonzero ionization factor $a^{(\mathrm{ion})}_{+1}$.

Analysis of ionization and tunneling factors allows us to conclude that the initial state with $q=-1$ (having zero momentum projection on the direction of IR field polarization) gives a contribution only to the IR-induced HHG, while the initial state with $q=+1$ (having zero momentum projection on the direction of XUV field polarization) gives a contribution only to the XUV-initiated HHG.

The initial state symmetry affects the polarization properties of the emitted radiation, which are determined by the recombination dipoles. These dipoles can be obtained from Eq. (26) by complex conjugation and further substitution of $\boldsymbol{K}'_j\to\boldsymbol{K}_j$ for the XUV-initiated HHG channel and $\boldsymbol{K}'_j\to\tilde{\boldsymbol{K}}_j$ for the IR-induced HHG channel. Returning electron momentum has one nonzero component along the IR field polarization vector so that the recombination dipole is oriented along the x axis (y axis) for the state with $q=-1$ ($q=+1$).

Taking into account that the state with $q=+1$ is orientated along the y axis and the state with $q=-1$ is orientated along the x axis, the role of initial state symmetry can be summarized as follows: (i) the HHG process is initiated by the field with a polarization vector parallel to the orientation of the initial state; (ii) the polarization of the generated harmonics from oriented states coincides with the polarization of the field initiating the HHG process (for $q=-1$, harmonics are polarized along the x axis, while generated harmonics are linearly polarized along the y axis for the initial state with $q=+1$).

The total field-induced dipole (summed in polarization) can be presented as

$$\boldsymbol{\mathcal{D}}(\Omega)\approx\tfrac{1}{3}[\hat{\boldsymbol{x}}(\hat{\boldsymbol{x}}\cdot\boldsymbol{\mathcal{D}}_{0,-1}(\Omega))+\hat{\boldsymbol{y}}(\hat{\boldsymbol{y}}\cdot\boldsymbol{\mathcal{D}}_{1,+1}(\Omega))], \tag{28}$$

where the corresponding components of the vector $\boldsymbol{\mathcal{D}}_{n,q}(\Omega)$ are given by Eqs. (9) and (10). The total HHG yield can also be presented as the sum of two terms:

$$\mathcal{Y}\approx\tfrac{1}{9}(\mathcal{Y}_x+\mathcal{Y}_y), \tag{29}$$

where $\mathcal{Y}_x$ ($\mathcal{Y}_y$) is the harmonic yield for a fixed harmonic polarization $\boldsymbol{e}_h=\hat{\boldsymbol{x}}$ ($\boldsymbol{e}_h=\hat{\boldsymbol{y}}$):

$$\mathcal{Y}_x=\frac{\Omega^4}{2\pi c^3}|\mathcal{A}(\Omega;\boldsymbol{e}_h=\hat{\boldsymbol{x}})|^2=\frac{\Omega^4}{2\pi c^3}|\boldsymbol{\mathcal{D}}_{0,-1}(\Omega)|^2, \tag{30}$$

$$\mathcal{Y}_y=\frac{\Omega^4}{2\pi c^3}|\mathcal{A}(\Omega;\boldsymbol{e}_h=\hat{\boldsymbol{y}})|^2=\frac{\Omega^4}{2\pi c^3}|\boldsymbol{\mathcal{D}}_{1,+1}(\Omega)|^2. \tag{31}$$

We note that in Eq. (28), we neglect the contribution of state with $q=0$. Indeed, the state $q=0$ is oriented along the z axis, i.e., perpendicular to IR and XUV fields, so that ionization and recombination steps are strongly suppressed. According to Eqs. (12) and (14) [see also Eq. (25)], the tunneling and ionization factors are zero within the presented semiclassical accuracy and the first order of perturbation theory in the XUV field. Suppression of the recombination step for state $q=0$ follows from the analysis above [see also Eq. (25)]. We also confirm the small contribution of the state with $q=0$ to HHG by numerical calculations (see next section).

III. NUMERICAL RESULTS AND DISCUSSIONS

In order to check the consistency of our analytical predictions for the laser-induced dipole moment in the two-color

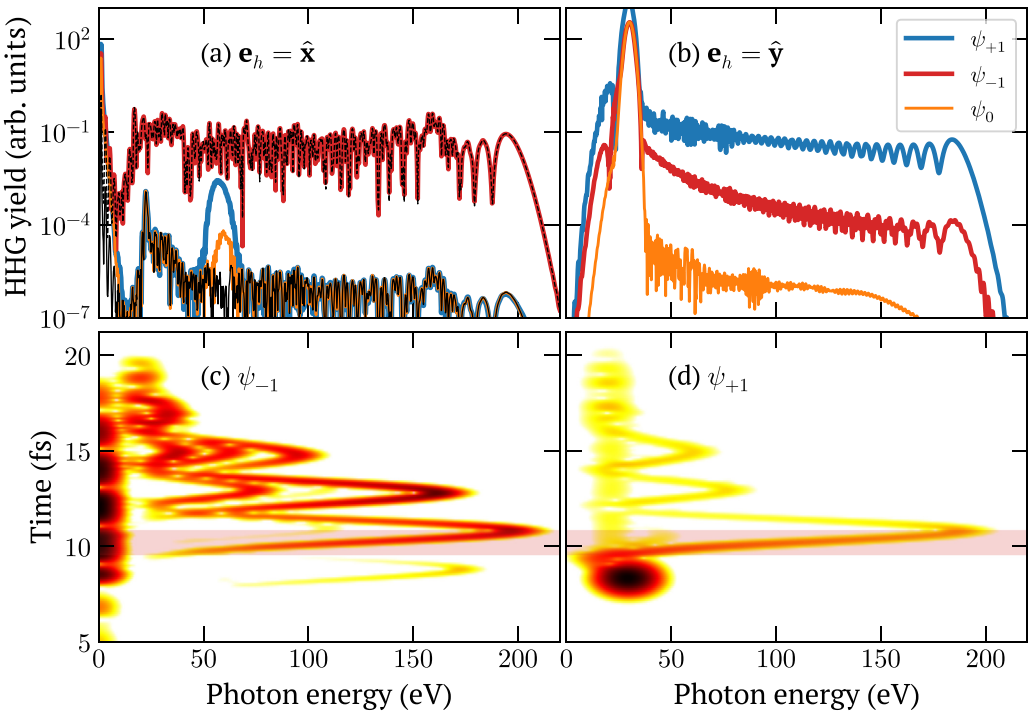

FIG. 1. HHG yield (35) for $\boldsymbol{e}_h = \hat{\boldsymbol{x}}$ (a) and $\boldsymbol{e}_h = \hat{\boldsymbol{y}}$ (b) calculated for the Ne atom subjected to the two-color field (1). Red lines: the yield from the initial state ψ_{-1}; blue lines: the yield from the initial state ψ_{+1}; orange lines: the yield from the initial state ψ_0. The dashed (solid) black line in (a) denotes the HHG spectra in the absence of the XUV pulse from the initial state ψ_{-1} (ψ_{+1}). The IR pulse parameters: $\mathcal{T}_{\rm IR} = 20$ fs [see Eq. (32)], $\omega_{\rm IR} = 1$ eV, and peak intensity $I_{\rm IR} = cF_{\rm IR}^2/(8\pi) = 4 \times 10^{14}$ W/cm^2 [see Eq. (2)]. The XUV pulse parameters: $\mathcal{T}_{\rm XUV} = 0.55$ fs [see Eq. (33)], $\omega_{\rm XUV} = 30$ eV, and peak intensity $I_{\rm XUV} = cF_{\rm XUV}^2/(8\pi) = 4 \times 10^{13}$ W/cm^2 [see Eq. (2)]. The time delay is $\tau = 8.3$ fs. Panels (c) and (d), respectively, show the Gabor transformation of $(\mathbf{a}_{-1} \cdot \hat{\boldsymbol{x}})$ from (a) and $(\mathbf{a}_{+1} \cdot \hat{\boldsymbol{y}})$ from (b).

field (1), we numerically solve the three-dimensional time-dependent Schrödinger equation (3D TDSE) in a single-active electron approximation (see the details in the Appendix). The IR component of the two-color field (1) was parametrized within the $\sin^2$ envelope:

$$f_{\rm IR}(t) = \begin{cases} \sin^2(\pi t/\mathcal{T}_{\rm IR}) & t \in [0, \mathcal{T}_{\rm IR}] \\ 0 & \text{otherwise,} \end{cases} \tag{32}$$

where $\mathcal{T}_{\rm IR}$ is the full duration of the IR pulse. The envelope of the XUV pulse was chosen in terms of the Gaussian function:

$$f_{\rm XUV}(t) = \exp\left[-2\ln(2)\, t^2/\mathcal{T}_{\rm XUV}^2\right], \tag{33}$$

where $\mathcal{T}_{\rm XUV}$ is the full-width at half maximum of intensity. The time delay between IR and XUV components is varied from 0 to $\mathcal{T}_{\rm IR}$.

The 3D TDSE was solved with the initial condition, which corresponds to the laser field-free state ψ_q for the Ne atom.[2] The numerically obtained time-dependent wave function is further utilized for the calculation of the Fourier transform of the dipole acceleration $\boldsymbol{a}_q$:

$$\boldsymbol{a}_q(\Omega) = \int \boldsymbol{a}_q(t) e^{i\Omega t} dt, \quad q = 0, \pm 1, \tag{34}$$

which was calculated for the initial state ψ_q [see Eq. (4)]. We note that there is a connection between acceleration and the dipole moment: $\boldsymbol{a}_q(\Omega) = -\Omega^2 \boldsymbol{\mathcal{D}}_q(\Omega)$. The probability of harmonic generation with frequency Ω and polarization vector $\boldsymbol{e}_h$ is calculated as

$$\mathcal{Y}_q(\Omega, \boldsymbol{e}_h) = \frac{|\boldsymbol{a}_q(\Omega) \cdot \boldsymbol{e}_h^*|^2}{2\pi c^3}, \quad q = 0, \pm 1. \tag{35}$$

In Fig. 1(a), we present the dependence of $\mathcal{Y}_{\pm 1}(\Omega, \boldsymbol{e}_h)$ and $\mathcal{Y}_0(\Omega, \boldsymbol{e}_h)$ on the harmonic frequency for $\boldsymbol{e}_h = \hat{\boldsymbol{x}}$. The numerical calculations of the harmonic yield (35) for $\boldsymbol{e}_h = \hat{\boldsymbol{x}}$ confirm our theoretical prediction; namely, linearly polarized harmonics generated from the initial state ψ_{-1} are fully determined by the laser-induced dynamics caused by the IR pulse (compare red solid line with black dashed line). Linearly polarized harmonics that came from the initial state ψ_{+1} have five orders of magnitude smaller intensity [see blue line in Fig. 1(b)]. The dynamics describing the generation of linearly polarized harmonics from the state ψ_{+1} is the same as for HHG in a linearly polarized field from a state having a nonzero magnetic projection on the polarization vector of the laser field. Within the semiclassical picture of HHG consisting of three steps—tunneling, propagation, and recombination—the HHG process from the initial states ψ_{+1} and ψ_0 is significantly suppressed by the tunneling and recombination steps.

Our numerical calculations show a resonant-like peak near $\Omega = 60$ eV. The resonant-like peak is placed near $\Omega = 2\omega_{\rm XUV}$, and thus is associated with the generation of the second harmonic of the XUV pulse by the IR-dressing atom [41]. According to the dipole selection rule, the polarization of even

[2]We note that since Ne has six outer electrons, expression (7) should be multiplied by 6.

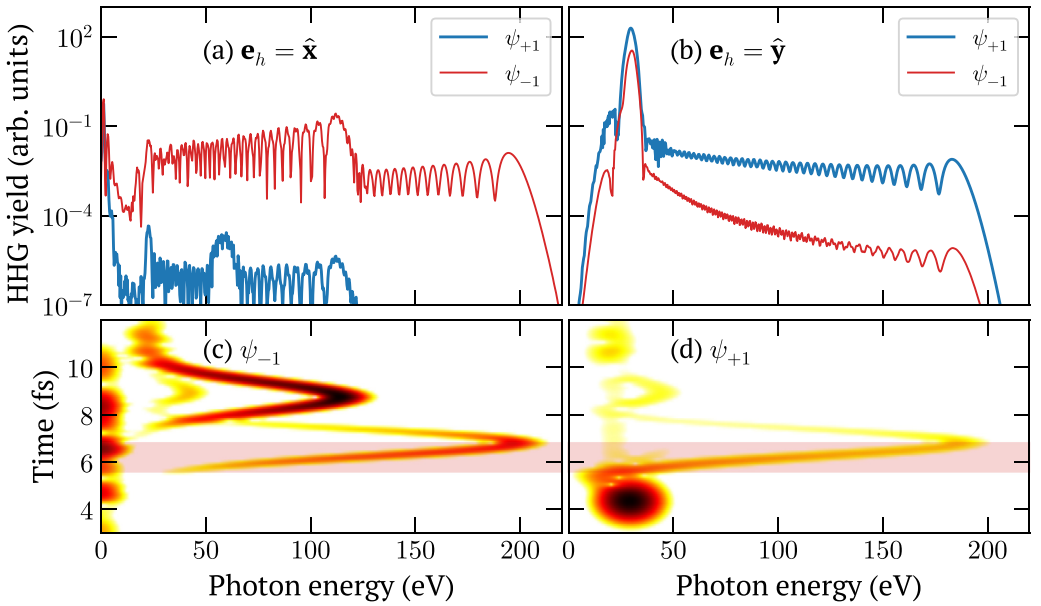

FIG. 2. HHG yield (35) for $\boldsymbol{e}_h = \hat{\boldsymbol{x}}$ (a) and $\boldsymbol{e}_h = \hat{\boldsymbol{y}}$ (b) calculated for the Ne atom subjected to the two-color field (1). Red lines: the yield from the initial state ψ_{-1}; blue lines: the yield from the initial state ψ_{+1}. IR pulse duration is $\mathcal{T}_{\rm IR} = 12$ fs, XUV pulse intensity is $I_{\rm XUV} = 4 \times 10^{12}$ W/cm^2, other parameters of IR and XUV pulses are the same as in Fig. 1. The time delay is $\tau = 4.3$ fs. Panels (c) and (d), respectively, show the Gabor transformation of $(\mathbf{a}_{-1} \cdot \hat{\boldsymbol{x}})$ from (a) and $(\mathbf{a}_{+1} \cdot \hat{\boldsymbol{y}})$ from (b).

harmonics of the XUV field coincides with the polarization of the IR field, whose polarization is perpendicular to the polarization vector of the XUV field.

The dependency of $\mathcal{Y}_{\pm1}(\Omega, \boldsymbol{e}_h)$ and $\mathcal{Y}_0(\Omega, \boldsymbol{e}_h)$ on the harmonic frequency for $\boldsymbol{e}_h = \hat{\boldsymbol{y}}$ is presented in Fig. 1(b). Contrary to the results in Fig. 1(a), the contribution from the initial state ψ_{+1} is dominant, while the generation of high-order harmonics from the state ψ_{-1} is suppressed by a few orders of magnitude. Moreover, the oscillation pattern and extension of the high-energy plateau in Fig. 1(b) is different from

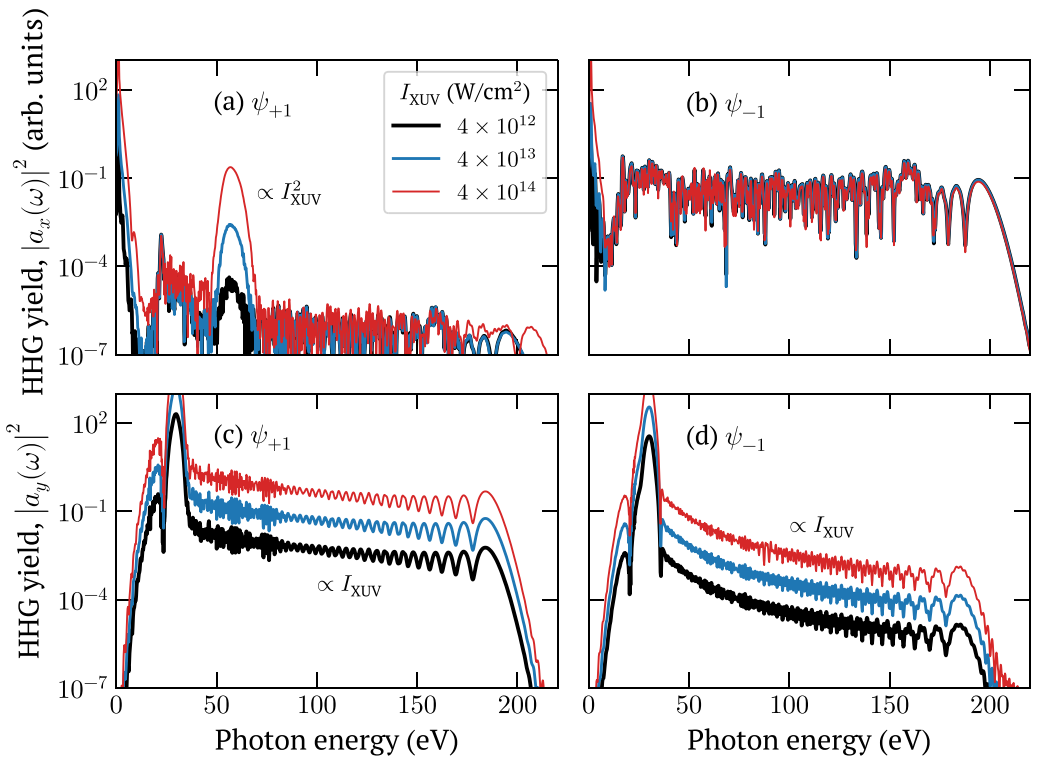

FIG. 3. HHG yield (35) for $\boldsymbol{e}_h = \hat{\boldsymbol{x}}$ (a and b) and $\boldsymbol{e}_h = \hat{\boldsymbol{y}}$ (c and d) calculated for the Ne atom subjected to the two-color field (1) with initial state ψ_{+1} (a and c) and ψ_{-1} (b and d). Red lines: $I_{\rm XUV} = 4 \times 10^{14}$ W/cm^2; blue lines: $I_{\rm XUV} = 4 \times 10^{13}$ W/cm^2; black lines: $I_{\rm XUV} = 4 \times 10^{12}$ W/cm^2; other parameters of IR and XUV pulses are the same as in Fig. 1.

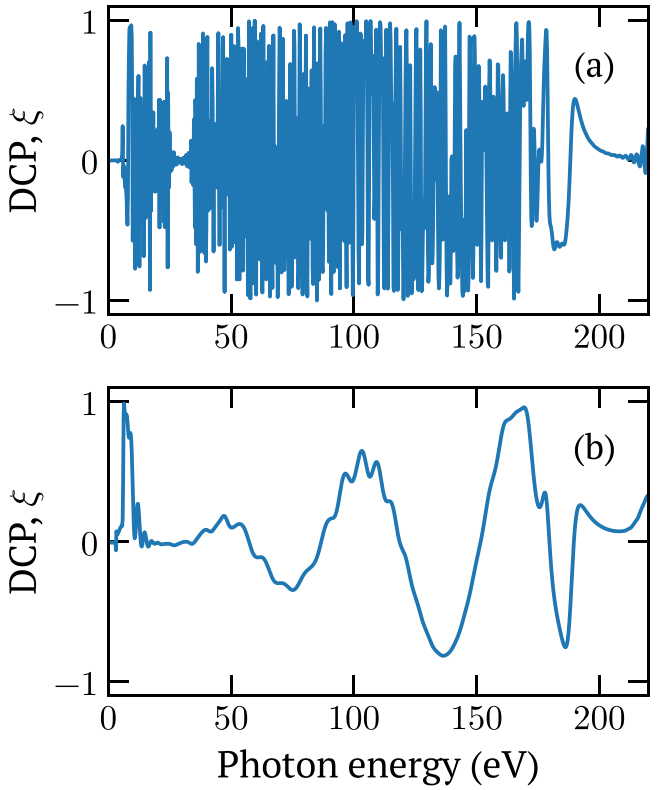

FIG. 4. The degree of circular polarization of harmonics as a function of harmonic energy Ω (a) for the raw harmonic yield and (b) for optimized harmonic yield originating from a single short trajectory. The parameters of the laser field are the same as in Fig. 1.

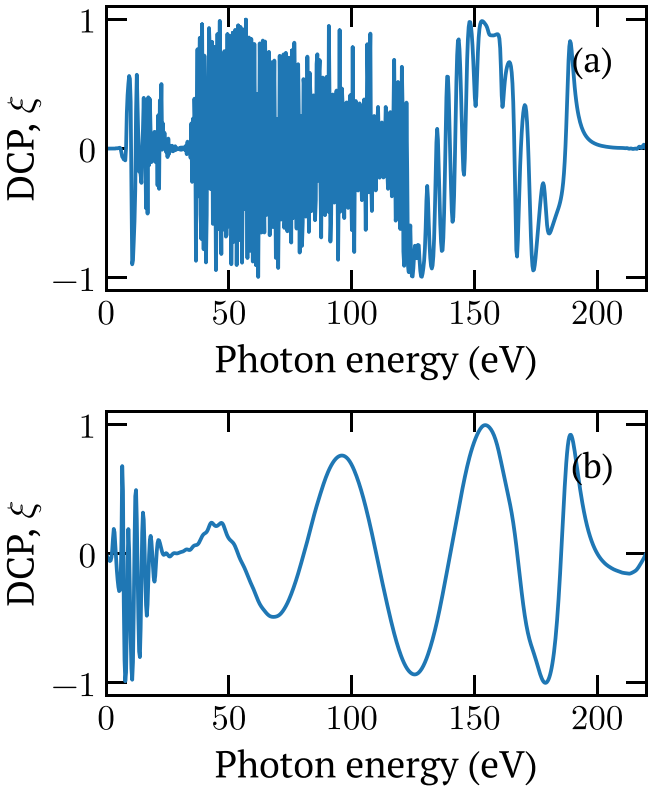

FIG. 5. The same as in Fig. 4 but for the parameters of the laser field as in Fig. 2.

that in Fig. 1(a), thereby eliminating a different physics in the formation of the high-energy harmonics in the two-color field (1) for initial states ψ_{+1} and ψ_{-1}. The main part of the high-energy plateau in Fig. 1(b) is formed by two trajectories, while the plateau in Fig. 1(a) is formed by four and more trajectories [see spectrogram in Figs. 1(c) and 1(d)]. Our numerical results show that linearly polarized harmonics with $\boldsymbol{e}_h = \hat{\boldsymbol{y}}$ that originate from the ψ_{-1} initial state have a much smaller intensity compared with the ψ_{+1} initial state, which confirms the validity of Eqs. (28). The resonant-like peak near $\Omega = 30$ eV is associated with the elastic scattering of the XUV pulse on the Ne atom [42]. The contribution of state with $q = 0$ is negligibly small, as in the case $\boldsymbol{e}_h = \hat{\boldsymbol{x}}$.

In Fig. 2 we present HHG spectra as in Fig. 1 but for the shorter duration of the IR pulse. The shortening of IR pulse duration leads to a decrease in the number of contributing closed electron trajectories. Part of high-energy HHG spectra is determined only by a single pair of short and long trajectories [43] [see harmonics with energy more than 125 eV in Fig. 2(a) and more than 50 eV in Fig. 2(b)], thereby forming the characteristic oscillation pattern in HHG yield caused by the interference between short and long trajectories. In Figs. 2(c) and 2(d) we present the Gabor transform, which confirms the contribution of single-pair short and long electron trajectories in the IR field. In order to clarify the perturbative character of the XUV field contributing to different HHG channels, we present in Fig. 3 HHG spectra (35) for different XUV field intensities. The XUV intensity is changed in the range $4 \times 10^{12} - 4 \times 10^{14}$ W/cm^2 corresponding to the IR intensity to explicitly show the validity of the first-order perturbation theory in the XUV field for the IR-dressed atom. The gradual increasing of the XUV intensity by order of magnitude shows that the generation of linearly polarized harmonics with $\boldsymbol{e}_h = \hat{\boldsymbol{x}}$ from the ψ_{+1} state is suppressed[3] [see Fig. 3(a)], while generation from the ψ_{-1} state is essentially independent of the XUV field intensity and determined by dynamics of the IR-induced HHG. As seen from Figs. 3(c) and 3(d), the HHG spectra for harmonics with polarization vector $\boldsymbol{e}_h = \hat{\boldsymbol{y}}$ are linearly scaled by XUV field intensity, thereby numerically justify Eq. (10).

Our theoretical and numerical analysis shows that x and y components of the HHG dipole moment are induced by two independent HHG channels, thereby allowing to affect the polarization properties of harmonic by controlling one of the channels, e.g., through the time-delay control between IR and XUV components. In Figs. 4(a) and 5(a), we show the degree of circular polarization (DCP) of emitted harmonic as a function of energy:

$$\xi(\Omega) = \frac{\mathcal{Y}_+^{(\mathrm{circ})}(\Omega) - \mathcal{Y}_-^{(\mathrm{circ})}(\Omega)}{\mathcal{Y}_+^{(\mathrm{circ})}(\Omega) + \mathcal{Y}_-^{(\mathrm{circ})}(\Omega)},$$
$$\mathcal{Y}_\pm^{(\mathrm{circ})}(\Omega) = \frac{|\boldsymbol{a} \cdot \boldsymbol{e}_\pm^*|^2}{2\pi c^3}, \quad \boldsymbol{a} = 2(\boldsymbol{a}_{+1} + \boldsymbol{a}_{-1}), \tag{36}$$

[3]Excluding the "narrow" region of second harmonic generation of the XUV field, whose intensity quadratically depends on XUV intensity.

where $\mathcal{Y}_{\pm}^{(\mathrm{circ})}$ is the partial yield of harmonic with left- and right-hand circular polarization, $\boldsymbol{e}_{\pm} = (\hat{\boldsymbol{x}} \pm i\hat{\boldsymbol{y}})/\sqrt{2}$. The DCP rapidly oscillates in the range from $+1$ to -1. The origin of these rapid oscillations is the interference of many partial amplitudes associated with electron trajectories contributing to the x component of the laser-induced dipole. The number of contributed trajectories can be reduced by decreasing the duration of the IR pulse. Indeed, for $\Omega > 125$ eV [see Fig. 5(a)], the small-scale oscillations are caused by interference between short and long trajectories in the IR-induced dipole moment, while large-scale oscillation in Fig. 5(a) is determined by a short trajectory. In order to smooth the rapid oscillations in the energy dependence of DCP, it is necessary to reduce the number of contributed trajectories and thus separate the contribution of amplitudes related to the single short trajectory [see the pink blurred area in Figs. 1, 2(c), and 2(d)]. The number of contributed trajectories can be reduced by utilizing extremely short IR pulses with a duration near the one optical cycle [44–47], while short trajectory separation results from the propagation effects, and it is realized by satisfying phase-matching conditions [48–50].

As we pointed out above, harmonic polarization control can be realized by changing either the XUV pulse intensity and phase or the time delay between IR and XUV pulses. According to Eq. (10), the parameter τ affects both the phase of the y component of the laser-induced dipole through the exponential factor $e^{i\omega_{\mathrm{XUV}}\tau}$ and its amplitude through the XUV pulse envelope $f_{\mathrm{XUV}}(t_j' - \tau)$; therefore, the time delay may be an effective parameter for polarization control. Figure 6 shows the dependence of DCP on the harmonic frequency for different time delays (7.8 fs $< \tau <$ 8.8 fs). In Fig. 6, only amplitudes associated with short trajectories were taken into account. Our calculation shows that with the variation of time delay, the DCP of a fixed harmonic (see, e.g., $\Omega = 125$ eV) can be changed from -1 to $+1$, thereby realizing the polarization control.

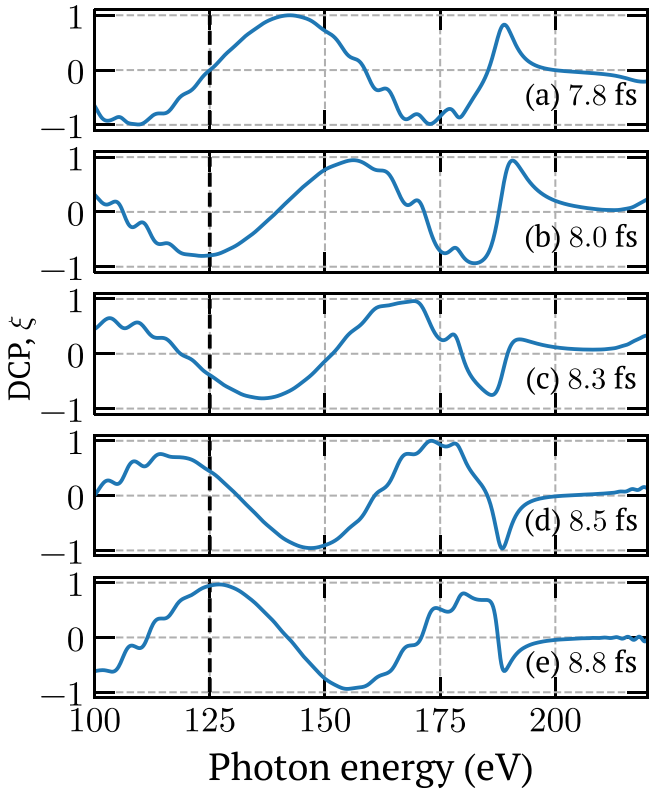

FIG. 6. The degree of circular polarization of harmonics as a function of harmonic energy Ω for optimized harmonic yield originating from a single short trajectory for different time delays (see figure for τ). The laser parameters are the same as in Fig. 1. Dashed lines mark the position of the harmonic with $\Omega = 125$ eV.

IV. SUMMARY

In this work, we have considered HHG from an atom interacting with the linearly polarized intense IR and synchronized perturbative XUV pulses, whose polarization vectors are mutually perpendicular to each other. An atom was considered within the assumption that active electrons are in p states. These triple-degenerate (in the projection of the angular momentum) states subjected to the two-color field are transformed to the "oriented" states, which are given by a superposition of states with different projections of the angular momentum and oriented along Cartesian unit vectors. We have shown that these states interact differently with orthogonal components of the two-color field by making it possible to separate different channels in the XUV-induced HHG. Our theoretical analysis, based on the analytical and numerical treatment of HHG, showed that harmonics generated from the state oriented along the IR polarization vector are formed according to the "classical" three-step scenario (tunneling, propagation, and recombination) driven by the IR field. Effects from the XUV component of the two-color field are negligibly small so that this state realizes IR-induced HHG in the absence of the XUV field. However, the state oriented along the XUV polarization vector realizes the XUV-initiated HHG channel, which also consists of three steps: XUV ionization, propagation in an intense IR field, with subsequent recombination. We have found that harmonics generated from the IR-induced HHG channel are linearly polarized along the IR polarization vector, while for the XUV-initiated HHG channel, generated harmonics are linearly polarized along the XUV pulse polarization vector. The aforementioned polarization properties make it possible to separate the XUV-initiated HHG channel from the IR-induced channel on a single-atom level by measuring harmonics with fixed polarization coinciding with XUV pulse polarization. We emphasize that this separation of channels in XUV-induced HHG is achieved without decreasing the IR field intensity, which is resorted in the collinear geometry of IR and XUV pulses [24–28].

We have discussed the polarization control of generated harmonics, which can be realized through the variation of the time delay between two components. Indeed, the laser-induced dipole moment is presented as a sum of vectors, which are mutually perpendicular to each other [see Eq. (28)]. The x component does not depend on the time delay and determines the amplitude for IR-induced HHG, while the magnitude and phase of the y component significantly depend on the time delay, thereby making possible polarization control through the time delay variation. Although polarization properties are rapidly changed with harmonic frequency, the

possible optimization for reducing these fast oscillations is suggested by separating partial HHG amplitudes associated with short trajectories. Within optimized HHG amplitudes, the time-delayed polarization control is more suitable for experimental realization. It should be noted that in this work we have considered a single-atom HHG and thereby neglected propagation effects, which may be crucial for two-dimensional laser fields (see Ref. [51] and references therein) and require a further challenged analysis.

ACKNOWLEDGMENTS

This work was supported by the Russian Science Foundation through Grant No. 22-12-00223.

APPENDIX: NUMERICAL SOLUTION OF THE 3D TDSE

We consider the dipole interaction of the Ne atom with the laser pulse (1). Our analysis is based on the numerical solution of the 3D TDSE in a single-active electron approximation:

$$i\frac{\partial}{\partial t}\psi_q(\boldsymbol{r},t)=\left[-\frac{1}{2}\nabla^2+V(r)+\boldsymbol{r}\cdot\boldsymbol{F}(t)\right]\psi_q(\boldsymbol{r},t), \quad \text{(A1)}$$

where $\psi_q(\boldsymbol{r},t)$ is the time-dependent electron wave function corresponding to the initial condition (4) at $t=0$, and $V(r)$ is the effective one-electron potential, which was found numerically by solving stationary Kohn-Sham equations for the Ne atom [52] using local density approximation with a self-interaction correction for the exchange-correlation potential [53]. The method of numerical solution of the 3D TDSE (A1) is based on the expansion of electron wave function in spherical harmonics [52,54]:

$$\psi_q(\boldsymbol{r},t)=r^{-1}\sum_{l=0}^{l_{\max}}\sum_{m=-l}^{l}\Psi_{lm}^{(q)}(r,t)Y_{lm}(\theta,\phi), \quad \text{(A2)}$$

where $\Psi_{lm}^{(q)}(r,t)$ is the radial part of the wave function $\psi_q(\boldsymbol{r},t)$ in the given orbital channel, $Y_{lm}(\theta,\phi)$ is the spherical harmonic, and θ and ϕ are the polar and azimuthal spherical angles, respectively, corresponding to the polar axis z.

Using expansion (A2), we reduce Eq. (A1) to the system of coupled equations:

$$\begin{aligned}i\frac{\partial}{\partial t}\Psi_{lm}^{(q)}=&\left[-\frac{1}{2}\nabla^2+V(r)\right]\Psi_{lm}^{(q)}+\\&+r\sqrt{\frac{2\pi}{3}}\sum_{l'=0}^{l_{\max}}\sum_{m'=-l'}^{l'}[-\tilde{F}^*(t)\langle lm|11|l'm'\rangle+\\&+\tilde{F}(t)\langle lm|1(-1)|l'm'\rangle]\Psi_{l'm'}^{(q)}, \quad \text{(A3)}\end{aligned}$$

TABLE I. The initial condition for the wave function $\Psi_{l=1,m}^{(q)}(r,t=0)$. For $l\neq 1$, $\Psi_{l,m}^{(q)}(r,t=0)\equiv 0$.

	$m=1$	$m=0$	$m=-1$
$q=1$	$i\phi_0(r)/\sqrt{2}$	0	$i\phi_0(r)/\sqrt{2}$
$q=0$	0	$\phi_0(r)$	0
$q=-1$	$-\phi_0(r)/\sqrt{2}$	0	$\phi_0(r)/\sqrt{2}$

where $\tilde{F}(t)=F_{\mathrm{IR}}(t)+iF_{\mathrm{XUV}}(t-\tau)$, $\langle lm|LM|l'm'\rangle=\int d\Omega Y_{lm}^* Y_{LM}Y_{l'm'}$ can be expressed in terms of Clebsch-Gordan coefficients $C_{a\alpha,b\beta}^{c\gamma}$:

$$\langle lm|LM|l'm'\rangle=\sqrt{\frac{(2L+1)(2l'+1)}{4\pi(2l+1)}}C_{l'0,L0}^{l0}C_{l'm',LM}^{lm}. \quad \text{(A4)}$$

The propagation of $\Psi_{lm}(r,t)$ over the time step Δt is performed by using three-split-operator symmetric decomposition together with the Crank-Nicolson method and the Numerov approximation following Sec. 4 in Ref. [55]. We use a nonuniform spatial grid, which has a higher density of nodes near the nucleus. The radial nodes of the spatial grid are specified as

$$r_k=k\Delta r+(\delta r/\Delta r-1)r_\alpha\tanh(k\Delta r/r_\alpha), \quad \text{(A5)}$$

where k is an integer; $\delta r=10^{-3}$ atomic units (au) is a tiny step of the radial grid, which is realized near the nucleus; $\Delta r=0.1$ au is the radial step for large distances; and $r_\alpha=20$ au is the scale for changing spatial step from δr to Δr. The size of the radial grid was limited by $R_{\max}=r_{\max}+\mathcal{R}_{\mathrm{abs}}$, where $r_{\max}=110$ au is the size of the simulation region and $\mathcal{R}_{\mathrm{abs}}=30$ au is the width of the multihump absorbing layer [56]. The time step is $\Delta t=0.02$ au, and maximum orbital momentum is $l_{\max}=192$.

The system of Eqs. (A3) is solved within the initial conditions given by Table I. The radial part of electron wave function $\phi_0(r)$ [see Eq. (4)] corresponds to the ground state of the $2p$ electron in a Ne atom. To find $\phi_0(r)$, we use propagation in the imaginary time of Eqs. (A3) for zero laser field and for some random initial wave function. The laser-induced dipole acceleration $\boldsymbol{a}_q(t)$ is calculated based on the Ehrenfest theorem:

$$\boldsymbol{a}_q(t)=-\mathbf{E}(t)-\int|\psi_q(\boldsymbol{r},t)|^2\nabla V(r)d\boldsymbol{r}. \quad \text{(A6)}$$

[1] T. Popmintchev, M.-C. Chen, P. Arpin, M. M. Murnane, and H. C. Kapteyn, The attosecond nonlinear optics of bright coherent X-ray generation, Nat. Photonics **4**, 822 (2010).

[2] T. Popmintchev, M.-C. Chen, D. Popmintchev, P. Arpin, S. Brown, S. Ališauskas, G. Andriukaitis, T. Balčiunas, O. D. Mücke, A. Pugzlys *et al.*, Bright coherent ultrahigh harmonics in the keV X-ray regime from mid-infrared femtosecond lasers, Science **336**, 1287 (2012).

[3] D. Popmintchev, B. R. Galloway, M.-C. Chen, F. Dollar, C. A. Mancuso, A. Hankla, L. Miaja-Avila, G. O'Neil, J. M. Shaw, G. Fan *et al.*, Near- and Extended-Edge X-Ray-Absorption Fine-Structure Spectroscopy Using Ultrafast Coherent High-Order Harmonic Supercontinua, Phys. Rev. Lett. **120**, 093002 (2018).

[4] P. Agostini and L. F. DiMauro, The physics of attosecond light pulses, Rep. Prog. Phys. **67**, 813 (2004).

[5] P. B. Corkum and F. Krausz, Attosecond science, Nat. Phys. **3**, 381 (2007).

[6] F. Krausz and M. Ivanov, Attosecond physics, Rev. Mod. Phys. **81**, 163 (2009).

[7] J. Itatani, J. Levesque, D. Zeidler, H. Niikura, H. Pépin, J. C. Kieffer, P. B. Corkum, and D. M. Villeneuve, Tomographic imaging of molecular orbitals, Nature (London) **432**, 867 (2004).

[8] H. J. Wörner, H. Niikura, J. B. Bertrand, P. B. Corkum, and D. M. Villeneuve, Observation of Electronic Structure Minima in High-Harmonic Generation, Phys. Rev. Lett. **102**, 103901 (2009).

[9] A. D. Shiner, B. E. Schmidt, C. Trallero-Herrero, H. J. Wörner, S. Patchkovskii, P. B. Corkum, J.–C. Kieffer, F. Légaré, and D. M. Villeneuve, Probing collective multi-electron dynamics in xenon with high-harmonic spectroscopy, Nat. Phys. **7**, 464 (2011).

[10] P. B. Corkum, Plasma Perspective on Strong Field Multiphoton Ionization, Phys. Rev. Lett. **71**, 1994 (1993).

[11] M. Lewenstein, P. Balcou, M. Y. Ivanov, A. L'Huillier, and P. B. Corkum, Theory of high-harmonic generation by low-frequency laser fields, Phys. Rev. A **49**, 2117 (1994).

[12] Y. Okajima, O. I. Tolstikhin, and T. Morishita, Adiabatic theory of high-order harmonic generation: One-dimensional zero-range-potential model, Phys. Rev. A **85**, 063406 (2012).

[13] M. V. Frolov, N. L. Manakov, A. A. Minina, A. A. Silaev, N. V. Vvedenskii, M. Y. Ivanov, and A. F. Starace, Analytic description of high-order harmonic generation in the adiabatic limit with application to an initial *s* state in an intense bicircular laser pulse, Phys. Rev. A **99**, 053403 (2019).

[14] A. V. Flegel, N. L. Manakov, I. V. Breev, and M. V. Frolov, Adiabatic expressions for the wave function of an electron in a finite-range potential and an intense low-frequency laser pulse, Phys. Rev. A **104**, 033109 (2021).

[15] R. Bartels, S. Backus, E. Zeek, L. Misoguti, G. Vdovin, I. P. Christov, M. M. Murnane, and H. C. Kapteyn, Shaped-pulse optimization of coherent emission of high-harmonic soft x-rays, Nature (London) **406**, 164 (2000).

[16] G. Lambert, B. Vodungbo, J. Gautier, B. Mahieu, V. Malka, S. Sebban, P. Zeitoun, J. Luning, J. Perron, A. Andreev *et al.*, Towards enabling femtosecond helicity-dependent spectroscopy with high-harmonic sources, Nat. Commun. **6**, 6167 (2015).

[17] D. D. Hickstein, F. J. Dollar, P. Grychtol, J. L. Ellis, R. Knut, C. Hernández-García, D. Zusin, C. Gentry, J. M. Shaw, T. Fan *et al.*, Non-collinear generation of angularly isolated circularly polarized high harmonics, Nat. Photonics **9**, 743 (2015).

[18] P.-C. Huang, C. Hernández-García, J.-T. Huang, P.-Y. Huang, C.-H. Lu, L. Rego, D. D. Hickstein, J. L. Ellis, A. Jaron-Becker, A. Becker *et al.*, Polarization control of isolated high-harmonic pulses, Nat. Photon **12**, 349 (2018).

[19] A. Fleischer, Generation of higher-order harmonics upon the addition of high-frequency XUV radiation to IR radiation: Generalization of the three-step model, Phys. Rev. A **78**, 053413 (2008).

[20] T. S. Sarantseva, M. V. Frolov, N. L. Manakov, A. A. Silaev, N. V. Vvedenskii, and A. F. Starace, XUV-assisted high-order-harmonic-generation spectroscopy, Phys. Rev. A **98**, 063433 (2018).

[21] T. S. Sarantseva, M. V. Frolov, N. L. Manakov, A. A. Silaev, A. A. Romanov, N. V. Vvedenskii, and A. F. Starace, Attosecond-pulse metrology based on high-order harmonic generation, Phys. Rev. A **101**, 013402 (2020).

[22] T. S. Sarantseva, A. A. Romanov, A. A. Silaev, N. V. Vvedenskii, and M. V. Frolov, Waveform retrieving of an isolated attosecond pulse using high-order harmonics generation of the superimposed infrared field, Opt. Express **29**, 38298 (2021).

[23] T. S. Sarantseva, A. A. Silaev, A. A. Romanov, N. V. Vvedenskii, and M. V. Frolov, Time-frequency analysis of high harmonic generation using a probe XUV pulse, Opt. Express **29**, 1428 (2021).

[24] K. J. Schafer, M. B. Gaarde, A. Heinrich, J. Biegert, and U. Keller, Strong Field Quantum Path Control Using Attosecond Pulse Trains, Phys. Rev. Lett. **92**, 023003 (2004).

[25] J. Biegert, A. Heinrich, C. P. Hauri, W. Kornelis, P. Schlup, M. P. Anscombe, M. B. Gaarde, K. J. Schafer, and U. Keller, Control of high-order harmonic emission using attosecond pulse trains, J. Mod. Opt. **53**, 87 (2006).

[26] G. Gademann, F. Kelkensberg, W. K. Siu, P. Johnsson, M. B. Gaarde, K. J. Schafer, and M. J. J. Vrakking, Attosecond control of electron–ion recollision in high harmonic generation, New J. Phys. **13**, 033002 (2011).

[27] D. Azoury, M. Krüger, G. Orenstein, H. R. Larsson, S. Bauch, B. D. Bruner, and N. Dudovich, Self-probing spectroscopy of XUV photo-ionization dynamics in atoms subjected to a strong-field environment, Nat. Commun. **8**, 1453 (2017).

[28] M. Krüger, D. Azoury, B. D. Bruner, and N. Dudovich, The role of electron trajectories in XUV-initiated high-harmonic generation, Appl. Sci. **9**, 378 (2019).

[29] F. Brizuela, C. M. Heyl, P. Rudawski, D. Kroon, L. Rading, J. M. Dahlström, J. Mauritsson, P. Johnsson, C. L. Arnold, and A. L'Huillier, Efficient high-order harmonic generation boosted by below-threshold harmonics, Sci. Rep. **3**, 1410 (2013).

[30] P. K. Maroju, C. Grazioli, M. Di Fraia, M. Moioli, D. Ertel, H. Ahmadi, O. Plekan, P. Finetti, E. Allaria, L. Giannessi *et al.*, Attosecond pulse shaping using a seeded free-electron laser, Nature (London) **578**, 386 (2020).

[31] J. Troß, S. Pathak, A. Summers, D. Rompotis, B. Erk, C. Passow, B. Manschwetus, R. Boll, P. Grychtol, S. Bari *et al.*, High harmonic generation in mixed XUV and NIR fields at a free-electron laser, J. Opt. **24**, 025502 (2022).

[32] N. L. Manakov and A. G. Fainshtein, Quasistationary quasienergy states and convergence of perturbation series in a monochromatic field, Theor. Math. Phys. **48**, 815 (1981).

[33] N. L. Manakov, M. V. Frolov, B. Borca, and A. F. Starace, Multiphoton detachment of a negative ion by an elliptically polarized, monochromatic laser field, J. Phys. B: At. Mol. Opt. Phys. **36**, R49 (2003).

[34] E. A. Pronin, A. F. Starace, M. V. Frolov, and N. L. Manakov, Perturbation theory analysis of attosecond photoionization, Phys. Rev. A **80**, 063403 (2009).

[35] M. V. Frolov, N. L. Manakov, and A. F. Starace, Effective-range theory for an electron in a short-range potential and a laser field, Phys. Rev. A **78**, 063418 (2008).

[36] M. V. Frolov, N. L. Manakov, T. S. Sarantseva, and A. F. Starace, High-order-harmonic-generation spectroscopy with an elliptically polarized laser field, Phys. Rev. A **86**, 063406 (2012).

[37] T. S. Sarantseva, M. V. Frolov, N. L. Manakov, M. Y. Ivanov, and A. F. Starace, Harmonic generation spectroscopy with a

two-colour laser field having orthogonal linear polarizations, J. Phys. B: At. Mol. Opt. Phys. **46**, 231001 (2013).

[38] D. A. Varshalovich, A. N. Moskalev, and V. K. Khersonskii, *Quantum Theory of Angular Momentum* (World Scientific, Singapore, 1988).

[39] M. V. Frolov, N. L. Manakov, A. A. Minina, S. V. Popruzhenko, and A. F. Starace, Adiabatic-limit Coulomb factors for photoelectron and high-order-harmonic spectra, Phys. Rev. A **96**, 023406 (2017).

[40] N. L. Manakov, S. I. Marmo, and A. V. Meremianin, A new technique in the theory of angular distributions in atomic processes: The angular distribution of photoelectrons in single and double photoionization, J. Phys. B: At. Mol. Opt. Phys. **29**, 2711 (1996).

[41] A. A. Romanov, A. A. Silaev, N. V. Vvedenskii, I. V. Breev, A. V. Flegel, and M. V. Frolov, Second-harmonic generation of a short XUV pulse interacting with an IR-laser-dressed atom, Phys. Rev. A **106**, 063101 (2022).

[42] A. A. Romanov, A. A. Silaev, N. V. Vvedenskii, A. V. Flegel, and M. V. Frolov, Contribution of the collective electron dynamics to the polarization response of an atom subjected to intense IR and weak XUV pulses, Opt. Lett. **47**, 3147 (2022).

[43] M. V. Frolov, N. L. Manakov, A. M. Popov, O. V. Tikhonova, E. A. Volkova, A. A. Silaev, N. V. Vvedenskii, and A. F. Starace, Analytic theory of high-order harmonic generation by an intense few-cycle laser pulse, Phys. Rev. A **85**, 033416 (2012).

[44] J. Park, J.-H. Lee, and C. H. Nam, Generation of 1.5 cycle 0.3 TW laser pulses using a hollow-fiber pulse compressor, Opt. Lett. **34**, 2342 (2009).

[45] Y. Deng, A. Schwarz, H. Fattahi, M. Ueffing, X. Gu, M. Ossiander, T. Metzger, V. Pervak, H. Ishizuki, T. Taira *et al.*, Carrier-envelope-phase-stable, 12 mJ, 15 cycle laser pulses at 21 μm, Opt. Lett. **37**, 4973 (2012).

[46] C. Manzoni, O. D. Mücke, G. Cirmi, S. Fang, J. Moses, S.-W. Huang, K.-H. Hong, G. Cerullo, and F. X. Kärtner, Coherent pulse synthesis: Towards sub-cycle optical waveforms, Laser Photonics Rev. **9**, 129 (2015).

[47] P. Steinleitner, N. Nagl, M. Kowalczyk, J. Zhang, V. Pervak, C. Hofer, A. Hudzikowski, J. Sotor, A. Weigel, F. Krausz, and K. F. Mak, Single-cycle infrared waveform control, Nat. Photonics **16**, 512 (2022).

[48] P. Salières, A. L'Huillier, and M. Lewenstein, Coherence Control of High-Order Harmonics, Phys. Rev. Lett. **74**, 3776 (1995).

[49] P. Balcou, P. Salières, A. L'Huillier, and M. Lewenstein, Generalized phase-matching conditions for high harmonics: The role of field-gradient forces, Phys. Rev. A **55**, 3204 (1997).

[50] M. B. Gaarde, J. L. Tate, and K. J. Schafer, Macroscopic aspects of attosecond pulse generation, J. Phys. B: At. Mol. Opt. Phys. **41**, 132001 (2008).

[51] D. B. Milošević, Macroscopic effects in high-order harmonic generation–A focal-averaging method based on the integral solution of the wave equation, Opt. Express **30**, 12163 (2022).

[52] A. A. Romanov, A. A. Silaev, M. V. Frolov, and N. V. Vvedenskii, Influence of the polarization of a multielectron atom in a strong laser field on high-order harmonic generation, Phys. Rev. A **101**, 013435 (2020).

[53] D. Bauer and F. Ceccherini, Time-dependent density functional theory applied to nonsequential multiple ionization of Ne at 800 nm, Opt. Express **8**, 377 (2001).

[54] D. Bauer and P. Koval, Qprop: A Schrödinger-solver for intense laser–atom interaction, Comput. Phys. Commun. **174**, 396 (2006).

[55] D. Bauer, Qprop manual I. www.qprop.de (2005).

[56] A. A. Silaev, A. A. Romanov, and N. V. Vvedenskii, Multihump potentials for efficient wave absorption in the numerical solution of the time-dependent Schrödinger equation, J. Phys. B: At. Mol. Opt. Phys. **51**, 065005 (2018).